Remote Sensing of Environment 216 (2018) 586–597

Contents lists available at ScienceDirect

Remote Sensing of Environment

journal homepage: www.elsevier.com/locate/rse

Atmospheric correction of metre-scale optical satellite data for inland and coastal water applications

Quinten Vanhellemont*, Kevin Ruddick

Royal Belgian Institute of Natural Sciences, Operational Directorate Natural Environments, Gulledelle 100, Brussels 1200, Belgium

ARTICLE INFO

Keywords:
Remote sensing
Metre-scale resolution
Water colour
Water quality
Aerosol correction
Automation

ABSTRACT

A new atmospheric correction (AC) method for aquatic application of metre-scale resolution (MR) optical satellite imagery is presented in this article, and demonstrated using images from the Pléiades constellation. MR satellites are typically operated privately and imagery can be costly. However in recent years, the price of individual acquisitions has dropped and their revisit times have improved, making them promising tools for remote sensing of inland and coastal waters. Due to the spatial resolution requirements of these satellites, the bands on the sensors are relatively wide (60–140 nm on Pléiades) in order to achieve an acceptable signal to noise ratio. This bandwidth and the limited number of bands can pose problems for the AC as the water signal may not be negligible in any band, especially over turbid waters. Since the MR sensors have a relatively narrow swath (20 km for Pléiades) the atmosphere can generally be assumed to be homogeneous over a scene or subscene. This assumption allows the atmospheric path reflectance (ρ_{path}) to be estimated from multiple targets in the scene, which are selected according to the lowest observed top-of-atmosphere reflectances (ρ_{TOA}) in all bands. Rather than using pre-defined "dark" bands (e.g. in the NIR and SWIR) such as is common in other water-focused AC methods, the best band is selected automatically, i.e. the one yielding the lowest ρ_{path}. This criterion avoids unrealistic negative ("overcorrected") reflectances after the AC. Furthermore, for inland waters the NIR bands are usually affected by scattering from adjacent land and vegetation pixels, resulting in unrealistic ρ_{path} when used in the AC. The spatial resolution of the sensors is used as an advantage here, since ground-level object shadows (e.g. from trees and buildings) can be spatially resolved and are usually the pixels selected by the automated procedure for the determination of ρ_{path}. In fact, it is proposed that using these shadow pixels gives better performance than using any kind of water pixel for these broad-band MR sensors. The method is demonstrated using several Pléiades images, showing good performance in retrieval of the aerosol optical thickness (τ_a) for an urban (Brussels) and a coastal (Zeebrugge) site. Match-ups with water reflectances measured at the Zeebrugge AERONET-OC station show promising performance, although there is a significant spectral mismatch between the bands on the satellites and the CIMEL radiometer. Pléiades imagery of Zeebrugge reveals a turbid wake associated with the MOW1 measurement station, which opens perspectives of using MR satellites for the characterisation of monitoring and validation sites. Future work includes the application to other MR satellites (e.g. WorldView) and the evaluation for mass processing of open access high resolution (10–60 m) satellite data from Landsat and Sentinel-2.

1. Introduction

In the last few years the impacts of human activities on the coastal environment such as offshore construction and dredging have been directly observed from space with imagery from Landsat 8 (2013-present) and Sentinel-2 (2015-present). These missions were designed for land applications, but they sparked a new interest from the water quality remote sensing community for high resolution imagery, not only due to the improved radiometric quality compared to older comparable missions (Pahlevan et al., 2014; Franz et al., 2015), but also thanks to the open data policies employed by the space agencies. Landsat data are well-suited for turbidity mapping in the coastal zone (Vanhellemont and Ruddick, 2014), and has shown some promise for mapping chlorophyll-a concentration in phytoplankton dominated systems (Franz et al., 2015). Sentinel-2 has an additional band in the red-edge (at 705 nm), which allows for the estimation of chlorophyll-a absorption in the red band, and hence chlorophyll-a concentration in turbid waters (Chen et al., 2017; Toming et al., 2016; Vanhellemont

* Corresponding author.
E-mail address: quinten.vanhellemont@naturalsciences.be (Q. Vanhellemont).

https://doi.org/10.1016/j.rse.2018.07.015
Received 12 March 2018; Received in revised form 9 July 2018; Accepted 12 July 2018

and Ruddick, 2016), at unprecedented resolution. With the capability of retrieving chlorophyll-a concentration in the first nautical mile from the coast, Sentinel-2 can significantly contribute to the monitoring requirements of the European Union's Water Framework Directive and amendments (European Commission, 2000).

At the spatial resolution provided by these sensors (10–60 m) "new" processes can be resolved from space, such as dredging activities (Barnes et al., 2015; Vanhellemont and Ruddick, 2015a) and impacts of offshore construction (Vanhellemont and Ruddick, 2014). In the southern North Sea, shipwrecks were detected in Landsat 8 imagery by analysing turbid tidal wakes (Baeye et al., 2016). Turbid river plumes and estuaries can be analysed in more detail thanks to the high spatial resolution and robust atmospheric correction using shortwave-infrared bands (Brando et al., 2015; Ody et al., 2016; Novoa et al., 2017), and retrieval of various optically active constituents is possible (Concha and Schott, 2016; Olmanson et al., 2016). Intense cyanobacterial blooms have been widely studied using remote sensing data from MERIS (Kutser et al., 2006; Matthews et al., 2010; Wynne et al., 2010) and Landsat (Ho et al., 2017; Vincent et al., 2004). Recently, Landsat data were used to propose a link between the proximity to waters experiencing regular cyanobacterial blooms and the occurrence of Amyotrophic Lateral Sclerosis (ALS) (Torbick et al., 2017). The improved spatial resolution allows for analysis of aquaculture performance and perhaps impacts on the local environment (fish cages and their effects become spatially resolved). Using a combination of the optical and thermal bands on OLI, Landsat 8 data were used to assess suitability for oyster cultivation in estuaries in Maine (Snyder et al., 2017). Similarly, Sentinel-2 derived turbidity and chlorophyll-a concentration were used for studying the physiological response of oyster farms in the Bay of Bourgneuf (Gernez et al., 2017).

Metre-scale resolution (MR, < 1–5 m) satellite imagery (e.g. SPOT, IKONOS, RapidEye, WorldView) has been used for aquatic studies such as coral reef and bathymetry mapping (Stumpf et al., 2003; Hedley et al., 2016), dredging activities, sediment transport applications (Doxaran et al., 2006), and mapping of underwater vegetation (Mumby and Edwards, 2002; Roelfsema et al., 2014; Fritz et al., 2017). There is significant interest from the sediment transport modelling community for high resolution turbidity maps for model validation (Vanlede and Dujardin, 2014), and also from the ocean colour community for validation site characterisation (Vanhellemont and Ruddick, 2015b). Dorji and Fearns (2017) have shown that in regions of high variability and high turbidity the spatial resolution of the sensor is crucial to retrieve accurate estimates of the total suspended solids concentration (TSS). They observed a near seven-fold difference between the maximum TSS derived from WorldView-2 and Aqua/MODIS imagery (spatial resolution respectively 2 and 250 m). With their very high spatial resolution, MR satellites may bridge the gap between in situ, in essence point measurements, and larger scale pixel-averaged satellite observations. Imagery from MR sensors used to be very expensive, but it has dropped significantly in price in the last few years. It is expected to become more and more affordable, especially with the advent of commercial nano-satellite swarms (e.g. the "flocks" of Dove satellites by Planet Labs Ltd.), allowing for broader scale applicability to various problems, including remote sensing of water quality. The high resolution allows for the monitoring of small water bodies with which humans are in regular close contact (recreational or occupational).

The atmospheric correction (AC) of MR images often relies on external measurements of aerosol optical thickness (τ_a), or inputs of manual estimates of τ_a and a typical aerosol model (e.g. FLAASH, harrisgeospatial.com/docs/FLAASH.html). Other relatively crude methods are sometimes used, for example only correcting for Rayleigh scattering, or dark object subtraction (Chavez, 1988). Empirical Line methods estimate a linear relationship between satellite observations and the surface reflectance by using bright and dark (unvegetated and invariant) objects in the scene with known (i.e. measured) or modelled reflectance (Moran et al., 2001). The use of AC methods based on spectral relationships for Dark Dense Vegetation (Kaufman et al., 1997) is not possible for sensors that lack SWIR bands. Recently, a method using cast shadows has been proposed (Schläpfer et al., 2018) showing promise for MR imagery. In several cases, top-of-atmosphere imagery is used as-is. At present, no generic, automated and reliable atmospheric correction tools exist for water applications of MR imagery.

In this paper an automated AC scheme for MR optical satellite imagery is introduced, with good performance over turbid coastal and inland waters in mind. The scheme is entirely image based, and hence does not require external inputs such as τ_a estimates or measurements. The scheme was developed for the Pléiades constellation in particular, but is in essence generic, and can easily be adapted to other MR sensors. MR sensors usually do not have bands where the surface reflectance (ρ_s) is known for certain targets in contrast to Landsat and Sentinel-2 for example, which have SWIR bands (at 1.6 and 2.2 µm), where $\rho_s = 0$ for water, facilitating the AC of extremely turbid waters (Gao et al., 2007; Wang, 2007; Vanhellemont and Ruddick, 2015a). In the algorithm presented here, no band is selected a priori for the AC, and for each scene the "best" band is selected for determining the atmospheric path reflectance (ρ_{path}). Although in first instance good performance for water is the aim, reflectances for both land and water pixels are retrieved. Next to the description of the method, a first validation of the aerosol optical thickness retrieval with AERONET data, and of marine reflectance spectra from an AERONET-OC station is presented using several Pléiades images. The retrieval of water turbidity at very high spatial resolution in and around the port of Zeebrugge is demonstrated, as well as the capability of the method to retrieve spatial variability of τ_a for larger "full swath" images.

2. Data and methods

2.1. Satellite imagery

Pléiades is a two-satellite constellation that provides multi-spectral imagery at 2.8 m spatial resolution in four broad bands, and at 0.7 m in a panchromatic band (Table 1 and Fig. 1). Imagery is typically resampled to 2 m and 0.5 m by the satellite operator. The sensor has a swath width of 20 km, and due to pointability of the satellite, the constellation can offer near-daily revisit time with two satellites in orbit. Six images were used in this paper (see Table 2): two images covering Brussels, obtained from the Belgian Pléiades Archive (pleiades.busoc.be) and four images covering Zeebrugge ordered by RBINS from Airbus Defence and Space (intelligence-airbusds.com). Although this manuscript focuses on Pléiades imagery, the proposed

Table 1
Details on the Pléiades sensor bands. Note that the multispectral bands are typically resampled to 2 m and the panchromatic band to 0.5 m. The SNR lists the Pléiades A/B separately. The relative spectral responses are given in Fig. 1.

Band	Wavelength (nm)	Resolution (m)	F0 ($W\,m^{-2}\,\mu m^{-1}$)	SNR (at 100 $W\,m^{-2}\,sr^{-1}\,\mu m^{-1}$)
Pan	450–900	0.7	1915	152/161
Blue	450–520	2.8	1830	148/150
Green	520–600	2.8	1594	146/165
Red	630–690	2.8	1060	149/156
NIR	760–900	2.8	1548	188/183

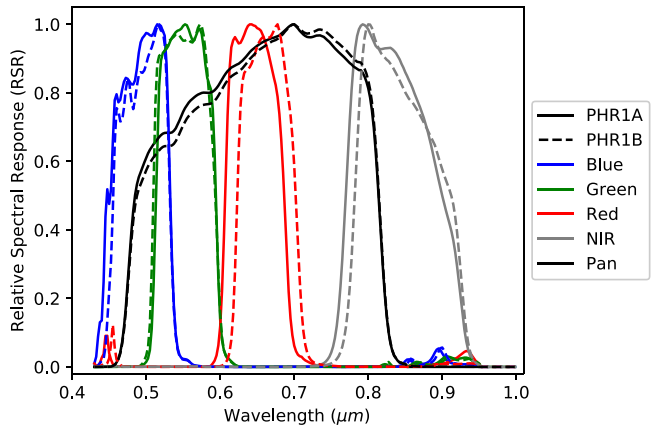

Fig. 1. Relative spectral response (RSR) of the bands on both Pléiades satellites: PHR1A (solid) and PHR1B (dashed).

atmospheric correction method is generic and applicable to other metre-scale resolution, broad-band satellite sensors.

2.2. In situ data

In situ measurements of aerosol optical thickness (τ_a) were obtained from the Brussels (at the Royal Meteorological Institute, RMI) and Zeebrugge (MOW1) AERONET stations for the six days for which imagery was available (see Table 2). Level 2 data were obtained from the AERONET website (http://aeronet.gsfc.nasa.gov), and τ_a was linearly interpolated to the time of satellite overpass (Table 2). To compare τ_a derived from the atmospheric correction with AERONET observations, the Brussels AERONET data were linearly interpolated to 550 nm from the bounding τ_a at 500 and 675 nm. The Zeebrugge AERONET station has an observation at 551 nm which was used as is.

The Zeebrugge AERONET station is equipped with a SeaPRISM water viewing radiometer (Zibordi et al., 2009), and provided water-leaving radiance measurements on three image dates (2014-07-17, 2014-09-08, and 2014-09-15). On 2014-09-15 the time difference between the satellite and the in situ measurement is > 2 h, which is significant in these turbid tidal waters, where temporal variability will influence the matchup performance. Non-f/Q corrected water-leaving radiances (L_w) were used as the standard f/Q correction based on chlorophyll-a concentration is not adequate for this turbid site. No generic turbid water f/Q correction methods exist for either in situ or satellite measurements. Due to multiple scattering in these turbid waters, the f/Q correction would be relatively small for the present study site. For mineral particle concentrations of 50–100 g m^{-3}, Vanhellemont et al. (2014) found a < 3% reflectance difference in the red SEVIRI band (560–710 nm) for a θ_v between 50° and 0°. The water-leaving radiances from the Level 2 data are converted to water-leaving radiance reflectances ($\rho_w = Rrs \cdot \pi$) by division by F0 (Thuillier et al., 2003) for a narrow 10 nm square band centred on the CIMEL wavelengths. ρ_w values are linearly interpolated to form a "hyperspectral" dataset which is then resampled to the relative spectral response (RSR) of the Pléiades bands. A band shifting method similar to the one presented by e.g. Mélin and Sclep (2015) and Zibordi et al. (2015) is not used, as it relies on either the knowledge of the IOPs, or the blue/green band ratio to estimate chlorophyll-a concentration - which are unknown, or is not applicable for the Zeebrugge site used here. Analysis of the CoastColour Round Robin simulated dataset (Nechad et al., 2015) indicates the resampled interpolated dataset based on the AERONET wavelengths will accurately estimate the blue channel, but will typically underestimate the green, red and NIR bands by 5–10%. See Supplementary data 3 for more details.

2.3. Atmospheric correction scheme

The atmospheric correction (AC) aims to separate the top-of-atmosphere (TOA) observation by the satellite sensor into the signal from the atmosphere and the signal from the surface in order to retrieve surface reflectances (ρ_s). The satellite image data were first transformed to TOA radiances (L_t) using the calibration coefficients provided in the image metadata. TOA reflectance (ρ_t) was then computed in each band:

$$\rho_t = \frac{\pi \cdot L_t \cdot d^2}{F0 \cdot \cos\theta_s}, \tag{1}$$

where d is the sun-earth distance in astronomical units (AU), $F0$ is the extraterrestrial solar irradiance (Table 1), and θ_s the solar zenith angle at the centre of the image.

To remove the impact of variable concentration of atmospheric gases, ρ_t is corrected for gas transmittance (t_g), here taken as the product of the band averaged ozone and water vapour transmittances:

$$t_g = t_{H_2O} \cdot t_{O_3}. \tag{2}$$

$t_{H_2}O$ is retrieved from a hyperspectral look-up table (LUT) generated using the radiative transfer model 6SV (Vermote et al., 2006; Kotchenova et al., 2006) for the scene centre sun and viewing zenith angles (θ_s and θ_v) and the total precipitable water ($u_{H_2}O$, in g/cm^2) and then resampled to the sensor and band specific relative spectral response (RSR). t_{O_3} is computed for the scene centre air mass according to

$$t_{O_3} = e^{-\tau_{O_3}(1/\cos\theta_s + 1/\cos\theta_v)}, \tag{3}$$

with τ_{O_3} the ozone optical thickness, obtained from

$$\tau_{O_3} = k_{O_3} \cdot u_{O_3}, \tag{4}$$

where u_{O_3} is the atmospheric ozone concentration in cm, and k_{O_3} (in cm^{-1}) is derived from the tabulated values distributed in the ocssw software distribution (seadas.gsfc.nasa.gov), resampled to the band specific RSR. Precipitable water and atmospheric pressure (P) are obtained from six hourly "reanalysis" MET files from the National Centers for Environmental Prediction (NCEP). Ozone concentration is obtained from the best available daily observations from the Ozone Monitoring Instrument (OMI) on AURA or the Total Ozone Mapping Spectrometer (TOMS) on Earth Probe (EP), with the Total Ozone Analysis using SBUV/2 and TOVS (TOAST) dataset used as fallback. (Note that no fallback data was required in the present study.) Necessary datasets are

Table 2
Pléiades imagery used in this paper. Data sources are the Belgian Pléiades Archive (BPA) or acquisitions ordered by RBINS. $\Delta\phi$ is the relative azimuth between the sun and sensor, with $\Delta\phi = 0$ viewing with the sun behind the satellite. The last two columns signify the availability of τ_a and L_w data from the Brussels and Zeebrugge-MOW1 AERONET stations. The AERONET-OC matchup for 2014-09-15 highlighted with (*) has a > 2 h time difference with the satellite image.

Date	Time (UTC)	Region	Scene	Satellite	θ_s (°)	θ_v (°)	$\Delta\phi$ (°)	Source	τ_a	L_w
2013-08-21	11:06	Brussels	FCGC600116235	PHR1A	39.2	19.9	15.5	BPA	Y	–
2015-06-05	10:43	Brussels	FCGC600310430	PHR1B	30.3	16.4	27.8	BPA	Y	–
2014-07-17	11:17	Zeebrugge	FCGC600225390	PHR1B	30.8	25.4	16.7	RBINS	Y	Y
2014-09-08	11:10	Zeebrugge	FCGC600252361	PHR1A	46.1	15.4	12.1	RBINS	Y	Y
2014-09-15	11:06	Zeebrugge	FCGC600252362	PHR1A	48.8	9.0	12.2	RBINS	Y	Y (*)
2014-09-21	11:10	Zeebrugge	FCGC600254111	PHR1B	50.9	14.3	9.7	RBINS	Y	N

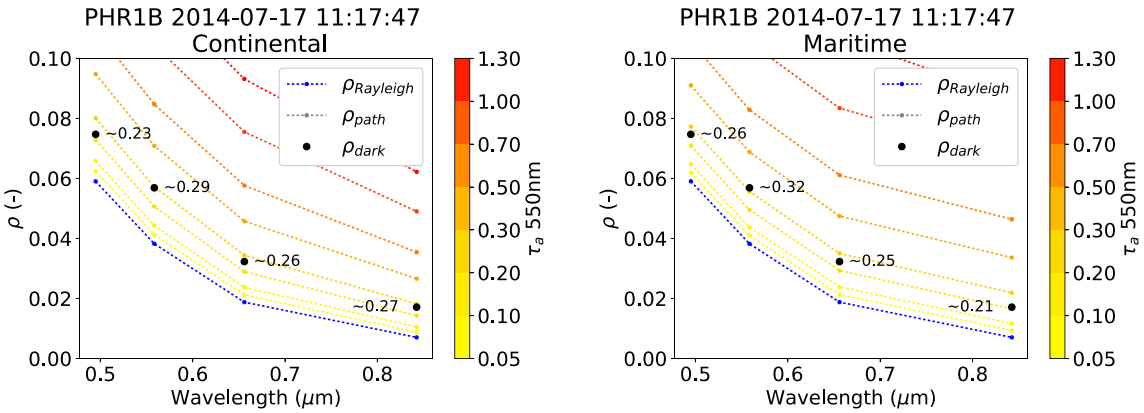

Fig. 2. The gas transmittance and sky reflectance corrected ρ_{dark} (black dots) retrieved from the 2014-07-17 Zeebrugge image, and ρ_{path} (yellow-red dashed lines) retrieved from the LUT for a range of τ_a and the (left) continental, and (right) maritime aerosol models. The Rayleigh reflectance is plotted in blue. For each band the linearly interpolated τ_a is plotted next to the ρ_{dark}. (For interpretation of the references to colour in this figure legend, the reader is referred to the web version of this article.)

automatically retrieved during processing from the NASA oceandata server (oceandata.sci.gsfc.nasa.gov). Both MET and ozone datasets are distributed as global grids with a one degree spacing in longitude and latitude, and are interpolated to the scene centre geographical coordinates. The six-hourly MET data were further interpolated to the time of satellite overpass. The atmospheric pressure at the time of overpass is used to resample the LUT used in the atmospheric correction scheme (see Section 2.4).

For water pixels, the diffuse sky reflectance reflected at the air-water interface is computed analytically (Gordon et al., 1988) and removed from the ρ_t observation:

$$\rho_{sky} = \tau_r \cdot p_r \cdot (4 \cos\theta_s \cos\theta_v)^{-1}, \quad (5)$$

where τ_r is the Rayleigh optical thickness, as retrieved from the LUT. θ_s and θ_v are the sun and viewing zenith angles, and p_r is given by

$$p_r = [r(\theta_s) + r(\theta_v)] \cdot P_r(\Theta), \quad (6)$$

where $r(\theta)$ is the Fresnel reflectance for air-incident rays:

$$r(\theta) = 0.5 \cdot \left\{ \frac{\sin^2(\theta - \theta_t)}{\sin^2(\theta + \theta_t)} + \frac{\tan^2(\theta - \theta_t)}{\tan^2(\theta + \theta_t)} \right\}, \quad (7)$$

with the angle of transmittance given by

$$\theta_t = \sin^{-1}\left(\frac{1}{n_w \sin\theta} \right), \quad (8)$$

where n_w is the refractive index of water with respect to air, taken as 1.34. P_r is the Rayleigh scattering phase function for a scattering angle Θ:

$$P_r(\Theta) = 0.75 \cdot (1 + \cos^2\Theta), \quad (9)$$

here taken as θ_+, which represents the photons that were reflected by the surface before or after scattering, with $\Delta\phi$ the relative azimuth between sun and sensor:

$$\cos(\theta_+) = \cos\theta_s \cos\theta_v - \sin\theta_s \sin\theta_v \cos\Delta\phi \quad (10)$$

For the purpose of automated, generic processing, the AC scheme needs to be fully image based and not require external inputs (e.g. τ_a measurements). The proposed method is based on two assumptions:

1. The atmosphere is homogeneous over a certain and limited spatial extent, i.e. the atmospheric path reflectance (ρ_{path}) is constant within the considered satellite scene or subscene.
2. There are pixels in the scene or subscene that have approximately zero surface reflectance ($\rho_s = 0$) in *at least one* of the sensor bands, representing an opportunity for estimating atmospheric path reflectance (ρ_{path}) in at least one band.

The atmospheric correction follows a multi-step process, where for each scene or subscene a "dark spectrum", ρ_{dark}, is first constructed from the ρ_t corrected for gas and air-water interface sky reflection. For each band, $\rho_{dark}(\lambda)$ is estimated in this manuscript by sorting the corrected ρ_t by brightness, and fitting an ordinary least squares regression (OLS) through the low reflectance end of the distribution (e.g. the darkest 1000 pixels). The intercept of the OLS regression is considered to be the best estimate of the "darkest" target in this band - while avoiding erroneous pixels (see Supplementary data 1 for an example). Note that the algorithm is not bound to this specific determination of the ρ_{dark}, and other methods (such as a percentile approach) could be used. The selected ρ_{dark} will be fitted to different aerosol models:

1. For the scene specific sun and viewing geometry, the $\rho_{path}(\lambda)$ is computed for a range of aerosol models and τ_a at 550 nm, based on a pregenerated LUT (see Section 2.4). For each band, and each of the aerosol types in the LUT, the observed $\rho_{dark}(\lambda)$ will be bound by two $\rho_{path}(\lambda)$ values, corresponding to τ_a steps in the LUT. These bounding τ_a values are then linearly interpolated to the $\rho_{dark}(\lambda)$ to give an estimated τ_a for this band and aerosol model.
2. For a given aerosol model, the τ_a estimate from the band giving the lowest non-zero τ_a will be used, as the higher values obtained using the other bands will give negative ρ_s for the dark pixels in that particular band.
3. The model and band combination giving the lowest overall τ_a will be used as the best estimate for a given ρ_{dark}. This choice was made as a result of the very limited band set of Pléiades. For sensors with a more extensive band set (e.g. Landsat 8/OLI or Sentinel-2/MSI), the lowest root-mean-squared difference (RMSD) between the ρ_{dark} and the estimated ρ_{path} for specific bands could be used instead to select between models.

This fitting procedure is illustrated in Fig. 2 for the 2014-07-17 image over Zeebrugge. For each band and aerosol model τ_a 550 nm is estimated, and the overall lowest is selected. Typically the continental model will give lower τ_a in the visible bands (in this example the blue band) and the maritime in the red/near-infrared. In this example, the blue band gives the lowest τ_a for the continental model (0.23) and the NIR band for the Maritime model (0.21), and hence the Maritime model and the NIR band are selected to retrieve atmospheric correction parameters. The application to a scene (Brussels, 2015-05-06) strongly affected by adjacency effects is given in Fig. 3. In the ρ_{dark}, the effect from the nearby forest can be seen especially in the NIR band, but also

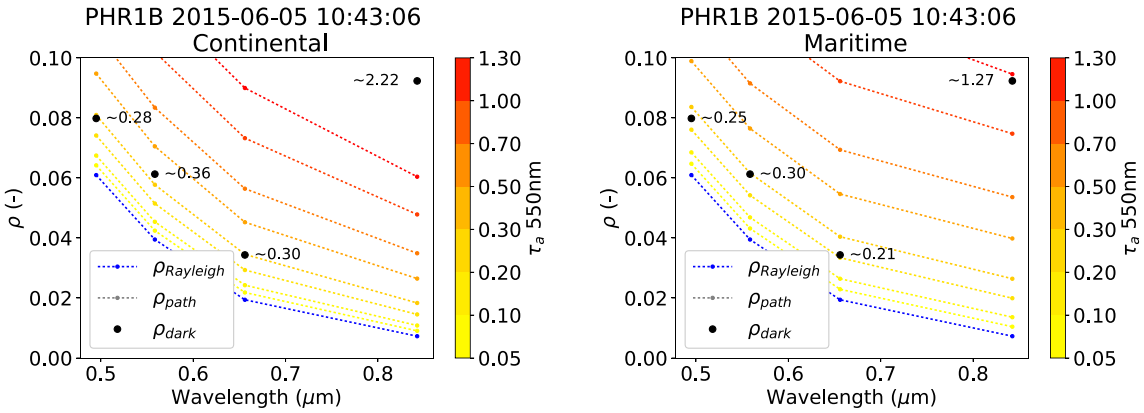

Fig. 3. Same as Fig. 2, but for a subscene over the Brussels Sonian Forest of the 2015-06-05 image. Here the ρ_{dark} is significantly affected by adjacency, which is especially visible in the NIR band. The algorithm will select in this case the blue or red bands for the continental and maritime models.

to some degree in the green band by the higher τ_a estimate. By fitting the ρ_{dark} to the LUT, a much larger τ_a is retrieved for the NIR band, and hence the NIR band will not be used in this case. By dynamically selecting the band, the adjacency effect is largely avoided in the aerosol correction, but will still be present in the retrieved ρ_s. The resulting ρ_s could potentially be corrected if an acceptable model is available (e.g. Sterckx et al., 2011), and possibly the magnitude of the adjacency effect could be estimated by the residual ρ_{dark}-ρ_{path} in the NIR band.

With the best fitting aerosol model and band combination selected, the parameters required for the atmospheric correction (see next section) are then retrieved for all bands using the computed τ_a at 550 nm:

- ρ_{path}: the atmospheric path reflectance,
- t_{du}: the two-way diffuse atmospheric transmittance,
- s_a: the spherical albedo of the atmosphere,

which allows for the computation of directional surface reflectance, ρ_s:

$$\rho_s = \frac{\rho_{pc}}{t_{du} + s_a \cdot \rho_{pc}}, \tag{11}$$

with ρ_{pc} the "path-corrected" reflectance:

$$\rho_{pc} = \frac{\rho_t}{t_g} - \rho_{path} - \rho_{sky}, \tag{12}$$

where t_g is the gas transmittance, and ρ_{sky} is an estimate of the air-water interface sky reflectance, which is set to 0 for land pixels and estimated analytically for water pixels from (Eq. (5)).

The contribution of sun and sky glint on wave facets is excluded from the atmospheric correction, as the wave facets, and hence glint, are assumed to be spatially resolved on the imagery and thus cannot be statistically modelled based on wind speed. Correction of wave facets on MR imagery is a challenging topic when there is no band with $\rho_s = 0$ over all water pixels (Lyzenga et al., 2006), and is out of the scope of the current manuscript.

The dark spectrum fitting (DSF) algorithm can be summarised in the following five steps:

1. The ρ_t is corrected for atmospheric gas transmittance and sky reflectance.
2. A ρ_{dark} is constructed, in the present paper we use the intercept of an OLS regression in each band (see Supplementary data 1).
3. τ_a at 550 nm is estimated using the ρ_{dark} in each band by interpolating the ρ_{path} for the different τ_a steps in the LUT.
4. For each aerosol model in the LUT, the band giving the lowest τ_a is retained.
5. The band and model combination giving the overall lowest τ_a is finally used in the processing.

2.4. Atmospheric correction LUT

A look-up table (LUT) is constructed using 6SV (Vermote et al., 2006; Kotchenova et al., 2006) containing atmospheric path reflectance, ρ_{path}, two-way diffuse atmospheric transmittance, t_{du}, and the spherical albedo of the atmosphere, s_a, at 14 wavelengths located in atmospheric transmittance windows (0.39, 0.41, 0.44, 0.47, 0.51, 0.55, 0.61, 0.67, 0.75, 0.865, 1.04, 1.24, 1.61, 2.25 μm), in order to minimise interpolation errors for typical satellite bands. The LUT is constructed for a range of sensor view zenith, sun zenith, and relative azimuth angles (see Supplementary data 2) for a black surface with no atmospheric gases (which are treated separately - see Section 2.3). The LUT was constructed for the standard 6SV continental, maritime, and urban aerosol models, but the latter is disabled from the model selection by default and should only be used in specific cases. The LUT is generic and can be flexibly updated with additional aerosol models if needed. Air-water interface effects were ignored as the table is intended to be used for high resolution satellites, where the waves are spatially resolved. Simulations were run for 3 atmospheric pressures, 500 mbar, 1013.25 mbar, and 1100 mbar, corresponding to an elevation range from about −500 to 5000 m. The LUTs are linearly interpolated during processing to the atmospheric pressure derived from ancillary MET data or the site elevation and a standard atmosphere.

For each sensor configured in the processor (currently PHR1A and PHR1B on both of the satellites in the Pléiades constellation) the LUT is interpolated from the 14 wavelengths to a hyperspectral (1 nm step) dataset between 0.39 and 2.25 μm. This hyperspectral dataset is then resampled to the relative spectral response (RSR) of the sensor bands. This approach allows for an easier addition of new satellites (such as WorldView) into the processor, without the need for computationally intensive LUT calculation. A comparison between simulation outputs using the sensor RSR and the 14 band interpolated values is given in Supplementary data 2.

3. Results

3.1. Retrieval of τ_a

Measurements of aerosol optical thickness (τ_a) were available from AERONET stations for all of the six images considered in this paper. Most images were bounded in time by AERONET τ_a measurements, except on 2014-09-21, where the Pléiades image was taken about 15 min after the last valid AERONET measurement of the day. The dark spectrum was retrieved from the full images (± 100 km^2) for Zeebrugge/MOW1, and from a small (± 5 km^2) subscene around the

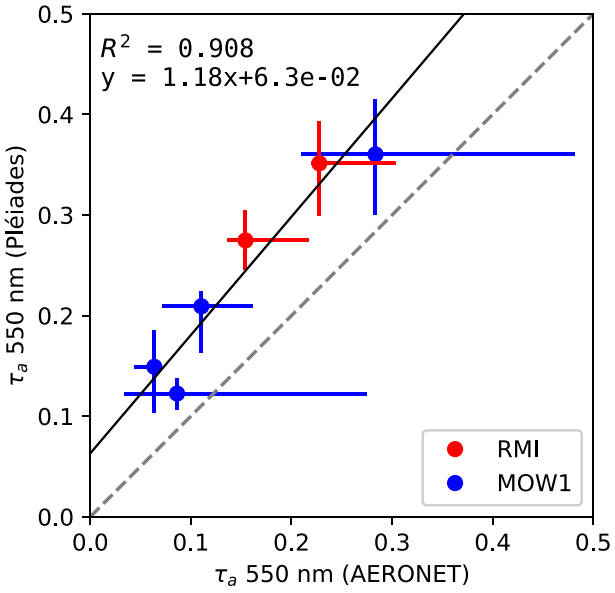

Fig. 4. Comparison of aerosol optical thickness (τ_a) at 550 nm measured at the AERONET stations and derived from six Pléiades images (Table 2). The blue and red colours represent the coastal Zeebrugge (MOW1) and urban Brussels (RMI) results, for which respectively a full scene and a subscene derived τ_a was used. The solid grey line is the Reduced Major Axis regression line. The dashed line shows the 1:1 line. The horizontal error bars represent the daily variability of the in situ τ_a and the vertical error bars the range of retrieved τ_a when randomly adding ± 5% in different bands at TOA (for 50 iterations). (For interpretation of the references to colour in this figure legend, the reader is referred to the web version of this article.)

station for Brussels/RMI. For these sites, these represent the best settings, which largely depend on the image extent and site surroundings (see Section 4). A scatter plot between the τ_a derived from the AERONET stations and the atmospheric correction procedure is given in Fig. 4, which shows that the method overestimates τ_a for all points, but achieves a good performance for the two study sites: R^2 of 0.91 and a Reduced Major Axis regression slope of 1.18 with low scatter. The daily variability of τ_a 550 nm at the AERONET stations on these six dates, and the timing of the Pléiades image and the τ_a value retrieved from the atmospheric correction scheme, is shown in Supplementary data 4.

3.2. Retrieval of ρ_w

Water reflectance measurements were available from the AERONET-OC station at Zeebrugge/MOW1 for three dates. On two dates (2014-07-17 and 2014-09-08) in situ measurements bound the satellite acquisition. For the third date (2014-09-15) there is a > 2-hour time difference between the in situ measurement and satellite overpass, and hence considerable differences between satellite and in situ were introduced because of tidal changes. No in situ data were available on the 2014-09-21, when the instrument was likely parked for bad weather conditions. For these scenes the τ_a was retrieved from the full scene, due to the relatively small extent of the scenes and the turbid waters around the site (see Section 4). Matchups were extracted centred on a location about 125 m north west of the actual location of the MOW1 platform, to avoid impacts of the reflectance of the structure itself and its shadow (Vanhellemont and Ruddick, 2015b), and of the surface sediment concentration in the tidal wake (see Section 3.3). The MOW1 structure itself has an impact mainly in the NIR band, while its shadow impacted all bands. The tidal wake shows typical characteristics of highly turbid waters, with mainly increased green, red and NIR reflectance. The mean, median and standard deviation were calculated from a 15 by 15 pixel box (corresponding to approximately a Landsat pixel) around the selected location. A comparison of the median spectra derived from Pléiades and from the AERONET-OC station is given in Fig. 5 for (a) the full atmospheric correction and (b) after only a Rayleigh correction (i.e. $\tau_a = 0$). For all three dates a strong linear correlation ($r \geqslant 0.95$) is found with a good match of the spectral shape. The best fit in terms of Root Mean Squared Difference (RMSD) is found for the images with bounding in situ observations. For these images the RMSD is 7.2×10^{-3} (2014-07-17), and 6.2×10^{-3} (2014-09-08), corresponding to about 10% of the visible band reflectances. For the last image (2014-09-15), the RMSD increases to 2.0×10^{-2}, or about 25% of the visible reflectances, which will be largely impacted by the tidal variability between in situ and satellite measurements. Spectral plots and the evolution of water reflectances in time for these three dates are given in Supplementary data 4. A scatter plot showing only the images

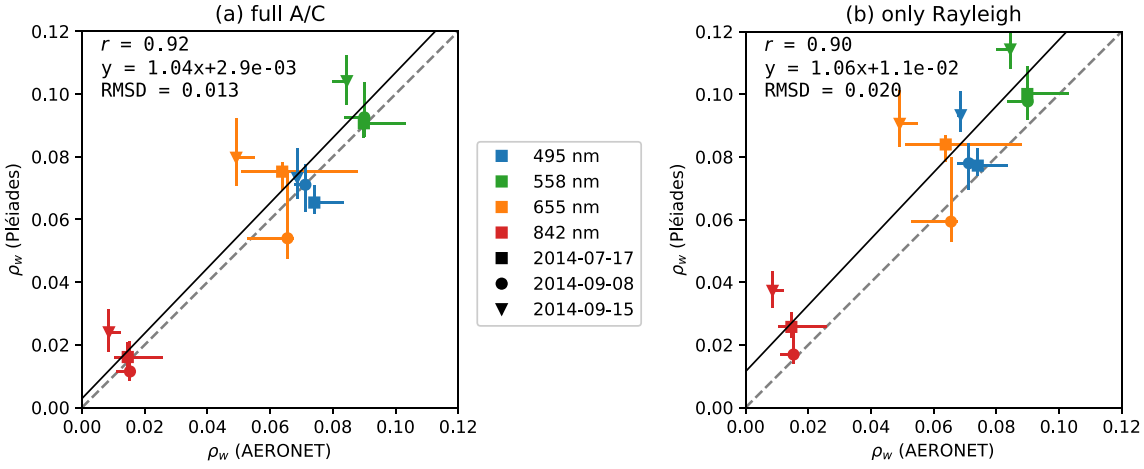

Fig. 5. Comparison of the water-leaving radiance reflectance (ρ_w) observed by the Zeebrugge (MOW1) AERONET-OC CIMEL SeaPRISM instrument and the retrieval from the Pléiades images for three dates: 2014-07-17 (squares), 2014-09-08 (circles), and 2014-09-15 (triangles). The left plot (a) shows the full atmospheric correction performed using the dark spectrum selection, and the right plot (b) shows the results after just a Rayleigh correction. The AERONET-OC data were linearly interpolated and resampled to the Pléiades bands. Pléiades points represent the median in a 15 by 15 pixel box (corresponding to about a Landsat pixel) located north-west of the station. The vertical error bars are the range of data in the 15 by 15 pixel box, and the horizontal error bars represent the daily in situ variability. The solid black line is the Reduced Major Axis regression line. The dashed grey line shows the 1:1 line. The time difference between the in situ measurement and the satellite overpass is > 2 h on 2014-09-15 (triangles), which mainly impacts the correlation coefficient and the offset of the regression line. Spectra for these dates are shown in Supplementary data 4.

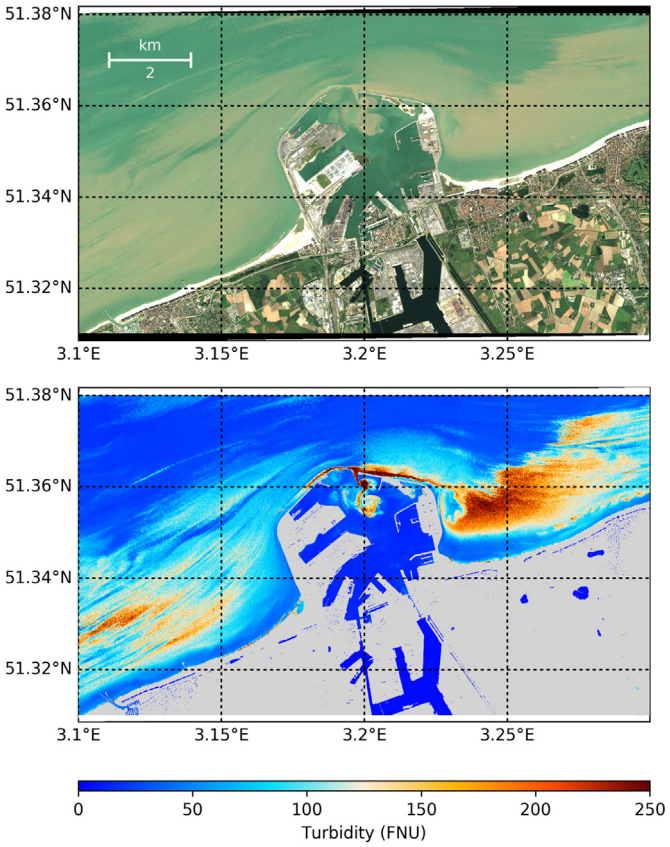

Fig. 6. RGB composite of ρ_s for the Zeebrugge image taken on 2014-09-08 (top) and turbidity product derived from the red band (bottom). Non-water pixels are masked in light grey, using thresholds on the retrieved surface reflectance (see Supplementary data 6).

with bounding in situ measurements is presented in Supplementary data 5.

3.3. Mapping of water turbidity

Water turbidity can be mapped using the red and NIR bands on Pléiades. Here we use the red band reflectance and the algorithm of Nechad et al. (2009) to retrieve turbidity in Formazine Nephelometric Units (FNU):

$$T = \frac{A \cdot \rho_w}{1 - \frac{\rho_w}{C}}, \tag{13}$$

where ρ_w is the water-leaving radiance reflectance, here taken as the ρ_s retrieved after atmospheric correction, and A and C are band specific calibration coefficients. These coefficients were recalibrated for Pléiades using collocated in situ measurements of above-water radiometry as described in Ruddick et al. (2006) and turbidity using a HACH 2100P turbidimeter (A = 294.49 FNU and C = 0.12495 for the red band, Bouchra Nechad, personal communication). Fig. 6 shows a ρ_s RGB composite and the derived water turbidity for the image taken on 2014-09-08. This image was taken during flood tide, with the current flowing in the northwest direction. This tidal current is the main source of sediment transport into the port, and it also creates a turbid wake around the MOW1 location. Both of these phenomena are shown in more detail in Fig. 7. This subset also shows a ship active in the port to dredge out these tidally displaced sediments and keep the port navigable. Non-water pixels were masked on the turbidity maps using a combination of thresholds (See Supplementary data 6). Certain low signal water targets (e.g. the inland docks, and other inland waters) prove to be difficult to reliably mask using spectral tests. The mask has some issues masking structure and building shadows (e.g. waterfront apartment building shadows), which have similar spectral characteristics to clear water pixels. Note also the shadows of the cranes, wind turbines, and the harbour walls on the subset in Fig. 7.

3.4. Spatial variability of the aerosol optical thickness

For the two large full swath images from the Belgian Pléiades Archive, a dark spectrum selected over a small subscene around the Brussels AERONET station gave a better τ_a retrieval, when compared to the in situ measurements (see Section 4.2.1). This suggests that it is possible to retrieve the spatial variability of aerosol concentration within these scenes using the method presented here. This is further demonstrated in Fig. 8 by tiled processing of one of the scenes over Brussels (2015-06-05), using subscenes of 500 × 500 pixels (approximately 1 × 1 km). For this processing, the AC and τ_a retrieval is run separately for each tile. Tiles with less than 10% valid pixels (i.e. certain tiles at the scene edges) are not processed to avoid selection of erroneous (i.e. non-dark) pixels in the ρ_{dark}. A higher τ_a (> 0.45) is found near the airport located Northwest of the city and along the canal and motorways crossing the city (± 0.35), and a lower τ_a (< 0.20) South and Southwest of the city, in the green Uccle suburb and the Sonian Forest.

4. Discussion

4.1. Atmospheric correction method

The assumptions made in the algorithm presented here are generally valid for very high resolution satellite images, as they usually cover a limited spatial extent, and can spatially resolve targets like tree and building shadows, or small absorbing water bodies. (Tree shadows on absorbing water pixels would make very strong dark targets!) The dark target assumption is similar to the “black NIR” (Gordon and Wang, 1994) or “black SWIR” (Wang and Shi, 2005; Gao et al., 2007; Wang, 2007) assumptions typically used in ocean colour processing, although the band selection is here performed dynamically and could as well include some “black VIS” pixels (Kutser et al., 2016). The method could also select dark land pixels (e.g. the aforementioned object shadows) if they are darker than any nearby water pixels. In fact, for most of the images presented here (4 out of 6 in Table 2), the use of shadow-on-land pixels provided better performance than the use of any kind of water pixel. A land-specific assumption such as fixed VIS-SWIR ratios for Dark Dense Vegetation (Kaufman et al., 1997) is not considered here, as in MR scenes with small spatial extent, and at this spatial resolution, ponds and object shadows are probably more prevalent than healthy and dense vegetation. In addition, the band set on many MR sensors does not include SWIR wavelengths. The results obtained in this study shows that on MR imagery “pure” shadow pixels from ground-level objects are often spatially resolved, and can provide a significant benefit for the atmospheric correction, similar to the findings by Schläpfer et al. (2018). While these shadows may not be truly black ($\rho_s = 0$), their surface signal is negligible compared to that of water targets, and hence they can be considered black for the estimation of atmospheric path reflectance.

4.2. Atmospheric correction performance

Despite the narrow swath of the sensor and the cost associated with image acquisition, collection of a number of matchups with in situ data was possible, thanks to the automated nature of the AERONET and AERONET-OC stations. The performance of the atmospheric correction scheme is evaluated based on matchups with τ_a measured by AERONET stations in two locations for six images, and with water reflectances measured by one AERONET-OC station near Zeebrugge for three images (of which two with closely timed bounding measurements). The results

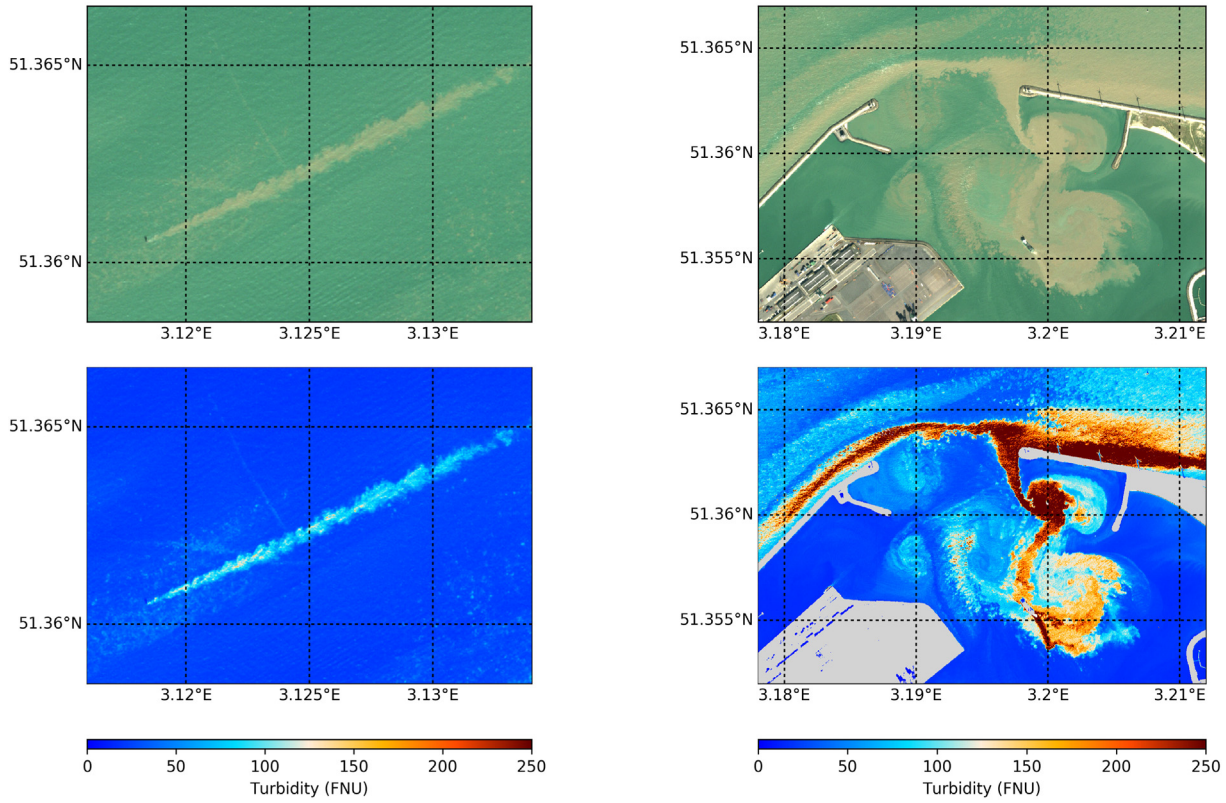

Fig. 7. Subsets of the RGB composite and turbidity product of Fig. 6 for (left) the MOW1 measurement pole and its turbid tidal wake, and (right) the Zeebrugge port entrance with tidal sediment inflow and a dredging ship.

from these two sets of matchups are discussed separately in the next subsections. A further validation may be performed in the future for which many more scenes around the world need to be collected. The code and LUTs for the atmospheric correction algorithm will be made freely available, and hence a community-based validation will be possible in the coming years.

4.2.1. Aerosol optical thickness retrieval

The accuracy of the aerosol optical thickness τ_a retrieval mainly depends on the presence of dark pixels in the scene and the spatial extent of the window in which it is determined. If there are no dark pixels (e.g. the turbid waters directly around the MOW1 site) the τ_a will be overestimated. If the window over the AERONET site is too large, pixels may be selected that do not represent the aerosol type or concentration directly over the site. For the Zeebrugge/MOW1 site, the entire images ($\pm$ 100 km^2) were used in order to include clearer offshore water pixels, and shadows over inland waters and land pixels. For the Brussels/RMI site, larger "full swath" scenes ($>$ 100 by 20 km) were obtained from the Belgian Pléiades archive, and a smaller subset was used ($\pm$ 5 km^2) centred around the site, due to the strong variability around the city centre of Brussels, the Sonian Forest and Zaventem Airport (see Section 4.3). As most MR images are acquired for a specific study over a relatively small spatial extent, the full scene approach should be sufficient for most applications. The satellite-retrieved τ_a is systematically larger than the one observed by the AERONET stations (Fig. 4), and this could be explained by the actual aerosol type not being exactly one of the two in the LUT. A more scattering aerosol for example would give a lower τ_a for the same ρ_{dark}, while still resulting in a similar ρ_{path}. Even with a more extensive range of aerosol models it may be impossible to distinguish between aerosol models due to the limits of the Pléiades band set. The overestimation of τ_a could also be related to the differences between satellite and in situ measurements (observations of backscattering/forward scattering), and the presence of a residual surface signal in the ρ_{dark} which increases the retrieved τ_a (see Section 4.4). The use of the band and model with the lowest retrieved τ_a can be sensitive to errors in atmospheric transmittance estimation (e.g. the O_2 absorption feature in the NIR band is currently ignored), but also to the presence of cloud shadows over dark targets, where it is possible that $\rho_{dark} \leqslant \rho_{Rayleigh}$, for which no τ_a can be computed. The high correlation coefficient shows that the retrieved τ_a is however highly related to the measured τ_a, and will hence give a reasonable estimate of the ρ_{path}, which leads to fulfilling the main aim of the atmospheric correction: retrieval of an accurate surface reflectance.

4.2.2. Water reflectance matchups

Water reflectance measurements were available from the Zeebrugge MOW1 AERONET-OC station for three dates for which we have Pléiades imagery (Table 2). For two dates, bounding in situ measurements were available, which were interpolated to the image time. For the third date, there was a significant $>$ 2-hour time difference between the satellite and the last available in situ measurement. Some uncertainty is associated with validating the broad bands of Pléiades with the narrow CIMEL bands, but we find very encouraging results: overall a good match is found between AERONET OC and Pléiades (Fig. 5). The largest discrepancy is found in the red band (655 nm), where the in situ measurement lacks the appropriate spectral coverage to accurately represent the observation in the Pléiades band.

This last matchup shows increased NIR, red and green reflectances, a typical signal of the resuspension of sediments during the tidal ebb flow. The blue band reflectance remains about the same, which can indicate turbid water reflectance saturation in this band. Apart from the blue band, the 2014-09-15 observations (triangles) are all above the regression line due to this large time difference and sediment resuspension. Removal of these points (see Supplementary data Fig. A10) increases the correlation coefficient and reduces the offset. A comparison is also made between using just a Rayleigh correction and a "full"

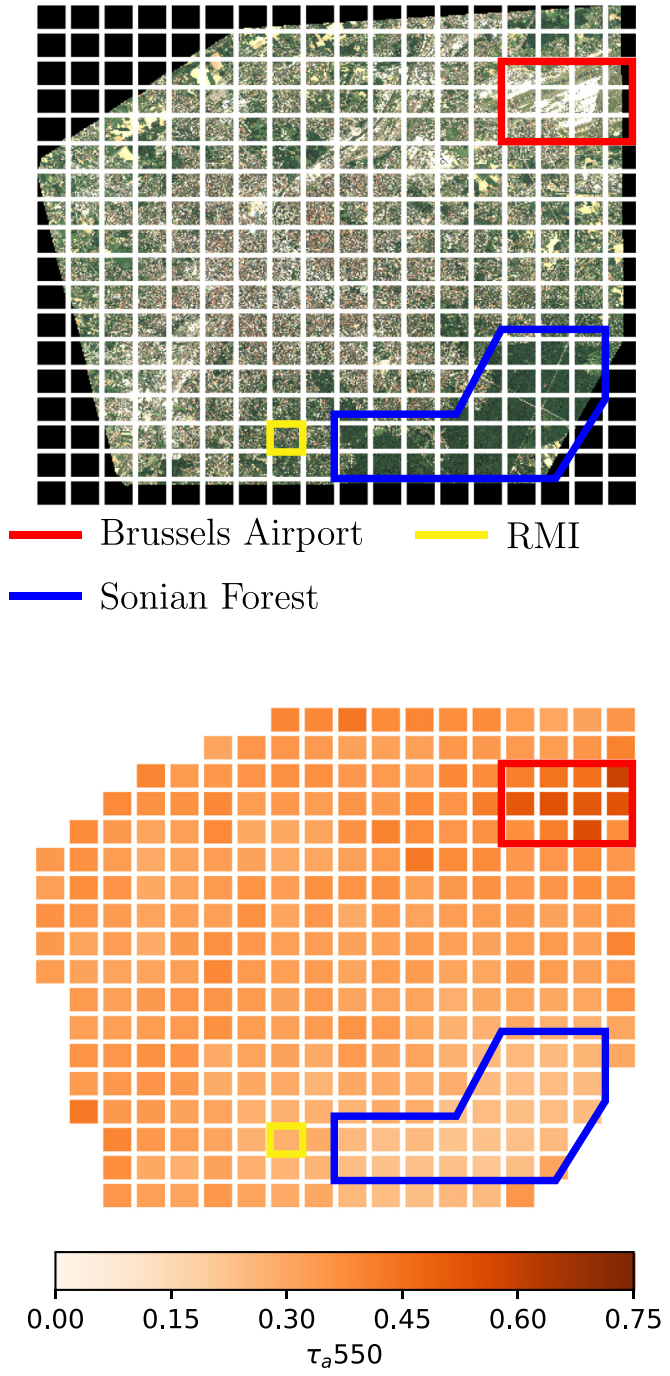

Fig. 8. Tiled processing of an image covering Brussels (2015-06-05), showing (top) the RGB composite and (bottom) the retrieved τ_a per tile. The tile containing Brussels/RMI AERONET station is highlighted in yellow, and the locations of Brussels Airport (Zaventem) and the Sonian Forest are annotated respectively in red and blue. (For interpretation of the references to colour in this figure legend, the reader is referred to the web version of this article.)

atmospheric path reflectance correction (Rayleigh + aerosols). The Rayleigh correction by itself gives a reasonable performance, but has a larger offset and RMSD due to the aerosol reflectance that has not been taken into account. Overall, the proposed aerosol correction gives better results than just a Rayleigh correction, and does not significantly overestimate the aerosol reflectance over these turbid waters. The NIR reflectance for these matchups is between about 0.01 and 0.015 (Fig. 5) and an AC assuming a dark NIR would significantly overestimate the aerosol reflectance (see also Section 4.4).

4.3. Tiled aerosol optical thickness retrieval

The larger "full-swath" images from the Belgian Pléiades Archive allowed for a tiled retrieval of τ_a. Mapping of the τ_a tiles for the 2015-06-05 Brussels image (Fig. 8) shows that especially in this varied urban environment the method is sensitive to spatial variability in aerosol concentration. Selected 500 × 500 pixel tiles covering the airport and the forest were manually inspected for the presence of dark shadows after processing, in order to assess the validity of the τ_a estimate. An overall brighter or darker surface in certain tiles can lead to higher or lower retrieved τ_a, but sufficient shadows were present in the tiles. The forest tiles showed a significant increase in NIR reflectance (due to healthy vegetation, see also Fig. 3) but a decrease in retrieved τ_a. Unfortunately there are no in situ τ_a measurements covering any spatial extent in the image available. However, a better correspondence with the Brussels/RMI AERONET measurements was found when using the tiled processing compared to the full scene processing. By interpolating retrieved values between the separate tiles, the effect of the tiling is minimised across the scene. If processing performance is not a constraint, then a moving tiling window could be used, with overlapping tiles providing a smooth estimate of the ρ_{path} across the scene.

4.4. Impact of the assumptions on ρ_{path} retrieval

As a result of the assumptions in the DSF, the ρ_{path} can be either (1) overestimated in the case of a non-zero ρ_s in the used band, or (2) underestimated in the case of unaccounted spatial variability of τ_a within the subscene. An increase in the subscene size will lead to a decrease in minimal ρ_t and hence to a decrease in estimated ρ_{path} for a given aerosol model. An overestimation of ρ_{path} will cause an underestimation of ρ_s and vice versa. In order to assess the impact of an error on the ρ_{path} estimation, the matchups presented in Fig. 5 were reprocessed with ± 0.1 and ± 0.2 on the retrieved τ_a, respectively giving relative errors of approximately 25–100 to 50–200% on our overall τ_a ranges. The results of this sensitivity analysis are presented graphically in Supplementary data 5. We find that an error in the τ_a estimation is represented by a white shift in the retrieved ρ_s, as indicated by the stable RMA slope and change in offset in the matchups with in situ data. The unmodified DSF and the $\tau_a - 0.1$ results return the best performance in terms of RMA offset and RMSD in this comparison. This indicates that the DSF can quite reliably split the ρ_t into ρ_s and ρ_{path}, but that there may be a slight overestimation of the τ_a due to residual surface signal in the ρ_{dark}.

In the case of a non-zero signal in the ρ_{dark} with the same absolute magnitude, the error on the ρ_{path} is largest for the NIR band and smallest for the blue band. The non-zero signal can be considered as an error on the ρ_t, and a range of ± 0.2 on the τ_a would represent a residual surface signal in the ρ_t of about 0.014 in the blue and 0.008 in the NIR band for the image presented in Fig; 2. By dynamically selecting the band used in the aerosol correction, the overestimation of ρ_{path} due to non-zero ρ_s in the ρ_{dark} is minimised by switching to shorter wavelength bands. Since the DSF uses the band and model combination giving the lowest τ_a, spatial variability within the subscene could cause an underestimation of ρ_{path}. By using a tiled processing as presented in Section 3.4, the errors of spatial variability should be significantly reduced. Over turbid waters, the tiled processing is however not recommended, as a more significant overestimation of the ρ_{path} due to the non-zero ρ_s in all bands may be introduced (see Section 4.2.2). Our results indicate that for the coastal site fixing the ρ_{path} over the scene (± 100 km^2) gives reliable results. It is thus likely that the spatial variability in the scene is less than the relative ranges tested for here, and that in our matchups the effect of a residual surface signal is larger than that caused by spatial variability of aerosols. This analysis shows results quite similar to the overestimation of τ_a found compared with in situ measurements (Fig. 4). However, despite the slight overestimation of τ_a, these results show the ρ_{path} and ρ_s are reliably estimated by the DSF.

4.5. Water turbidity retrieval

We have shown that satisfactory retrieval of water-leaving radiance reflectances from Pléiades imagery is possible, especially with the retrieval of water turbidity from the red band in mind. Hence, turbidity or related parameters such as the suspended sediment concentration can be derived at high spatial resolution. Some challenges remain for the use of these images, such as spatially resolved wave facets (i.e. varying fraction of sky glint), foam and floating debris. Human constructions and ships, and importantly their shadows, are also present. These effects are largely unavoidable for any sensor, but here very high resolution sensors could actually provide insights on the impact of these small features on coarser resolution satellite imagery and derived products.

Figs. 6 and 7 show examples of high resolution water turbidity maps derived from the 2014-09-08 image that are very useful for small scale sediment transport modelling and validation site characterisation. For example, the port of Zeebrugge is situated in very turbid waters and has to be regularly dredged to maintain accessibility. Modelling studies are ongoing on how the sediment transport into the port can be reduced, for example by the extension of existing or the construction of new harbour walls, to reduce the dredging effort. MR satellite imagery can provide the high resolution maps that are essential for the validation of these sediment transport models.

The high resolution of the imagery allows characterisation of the waters around MOW1 site, which is used as an ocean colour validation platform in the AERONET-OC network, and has been used as a reference site for many years. Both the platform structure itself and its in-water wake will impact data quality on coarser resolution sensors such as OLI, MSI, and OLCI (similar to the findings in Vanhellemont and Ruddick, 2015b). Furthermore, due to the high resolution of the sensor, the narrow MOW1 tidal plume is better resolved spatially, giving an improved estimate of the turbidity inside the plume (Fig. 7). Here we find a roughly four-fold increase of turbidity in the plume (~100 FNU) with respect to the ambient turbidity (~25 FNU). Other authors similarly found that the resolution of a sensor is crucial in order to detect these small scale, but significant, variations in turbidity (Dorji and Fearns, 2017). Unfortunately no direct turbidity measurements were available for the images presented here, but we expect these to be realistic retrievals since (1) the reflectance retrieval closely matches the AERONET-OC observation (Fig. 5), (2) the algorithm was calibrated using in situ measurements from extremely turbid waters around the world (including the Belgian Coastal Zone), and (3) the observed turbidity corresponds well to what is reported by Fettweis et al. (2016). The Pléiades turbidity is significantly higher than the one derived from the Landsat 8 scene 30 min earlier, due to the tidal resuspension of sediments in the half hour between observations (see Supplementary data 7). Autonomous turbidimeters are occasionally deployed offshore of Zeebrugge, and could aid in the validation of future image acquisitions. Note that during the ebb current the turbid tidal wake of the MOW1 structure (Fig. 7) extends to the west, and could occasionally enter the field-of-view of the AERONET-OC CIMEL.

5. Conclusions

- The atmospheric correction of very high resolution, broad band sensors without SWIR bands is a challenge. An automated method to estimate atmospheric path reflectance based on dark pixels found in the images (typically ground-level object shadows and water pixels) is presented. The dark pixels are selected avoiding erroneous pixels, and the most relevant spectral band and the optimal aerosol model are selected automatically based on minimum τ_a. For other sensors with more bands (notably in the SWIR), a goodness-of-fit test could be used to choose between models. The retrieval of τ_a is sensitive to residual signal in the final band used (the one giving lowest τ_a), and may be overestimated if the used target is not truly dark; e.g. in the case of glint on water pixels, or the presence of a surface signal in shadow pixels.
- The atmospheric path reflectance (ρ_{path}) was reliably retrieved for a series of six images of Brussels and Zeebrugge for which AERONET measurements were available. The τ_a was consistently overestimated, likely due to misrepresentation of the aerosol model and residual signal in the used shadow pixels. For the Brussels site, the τ_a retrieval significantly improved for smaller subscenes around the AERONET station, while in Zeebrugge a larger window was needed to include the appropriate dark pixels. Accurate ρ_s retrieval, not an accurate τ_a retrieval, is the main aim of the atmospheric *correction*. The high correlation between the in situ and satellite derived τ_a indicates however a decent performance of the algorithm. The water reflectance matchups further indicate that the ρ_{path} is adequately estimated.
- Due to the small swath, and typically small scene extent, a full scene fixed ρ_{path} is generally sufficient. Tiled processing of larger images provided a spatial map of aerosol optical thickness, showing variability even within the narrow Pléiades swath (20 km). For example, in the Brussels imagery a higher τ_a is found around Zaventem airport, while lower τ_a values are retrieved above the Sonian Forest. In comparison with the AERONET τ_a measurement at Brussels/RMI, better performance is found using a tiled processing, indicating some capabilities for resolving high resolution τ_a using ground-level object shadows.
- Two matchups with bounding water reflectances from the Zeebrugge AERONET-OC station show good performance of the sensor and atmospheric correction, with most of the uncertainty coming from the spectral mismatch between the satellite and in situ sensor bands. The CIMEL observations were interpolated and resampled to the Pléiades bands, and especially for the red band this can cause large errors due to spectral undersampling. A third matchup with increased temporal offset between satellite and in situ gives reasonable performance, but clearly shows effects of tidal resuspension and horizontal advection of sediments between the in situ measurement and the satellite image.
- A very high resolution turbidity map of the port of Zeebrugge was computed based on a Pléiades image, showing the sediment transport into the port during flood tide. This kind of map proves to be very useful for the validation of high resolution sediment transport models that are used to study coastal defence scenarios in order to reduce sediment inflow.
- Using very high resolution imagery the turbidity patterns around validation structures (in this case MOW1) and the effects of the structure itself could be studied. This allows for potential “reference” coordinates to be selected, excluding the direct structure impacts, and the effects of the flood or ebb tidal wakes. During ebb tide, the MOW1 tidal wake extends to the east, and could potentially enter the field of view of the CIMEL instrument. MR imagery of other autonomous validation stations or research vessels could reveal similar direct and indirect impacts on coarser resolution satellite pixels.

6. Future

- The algorithm performance needs to be evaluated for other sites such as inland waters, and waters in desert and ice covered sites. Flat homogeneous terrain with no water and no shadow-casting objects could be the most challenging test for the presented - and other - atmospheric correction algorithms. The algorithm performance over stable clear water sites should be examined to assess the performance under different illumination and atmospheric conditions. The algorithm and processor source code will be adapted to other sensors and will be publicly released in order to allow for a community based evaluation.
- The algorithm is generic and should be evaluated for similar (e.g.

WorldView) sensors, but also shows promise for certain coarser resolution sensors (e.g. Landsat 8/Sentinel-2), which have additional spectral bands (in the SWIR) that could improve the performance of the atmospheric correction. Due to their regular acquisition scheme, and free data access, these sensors will acquire more matchups with AERONET-OC data around the world, and could also be seen as test beds for evaluating different spectral band combinations. Similarly, the algorithm could be used for commercial imaging nanosatellite swarms. For coarser 'moderate' resolution ocean colour sensors (such as SeaWiFS, MODIS, MERIS, VIIRS, and OLCI), the algorithm performance would largely depend on the presence of black pixels in any band over various water targets. The algorithm would work over clear and mixed clear/turbid waters for most sensors, but would require the presence of SWIR bands to work over scenes with only turbid waters. With appropriate spectral coverage and signal-to-noise ratio, the algorithm could be applied to individual ρ_t spectra to allow "per pixel" processing over water.

- Validation with dedicated field campaigns is difficult due to the dynamic nature of aquatic systems, and the unpredictable timing of commercial satellite acquisitions. The use of autonomous systems is a preferred validation method. Ideally, the multispectral AERONET-OC network should be updated with hyperspectral instrumentation in order to validate any kind of satellite sensor, avoiding the need for band shifting of measurements. The band shifting performed here is relatively crude, but performs reasonably well. If inherent optical properties are available, more robust band shifting approaches could be applied.
- Further processing challenges include the surface waves and the sun and sky glint on the air-water interface that are spatially resolved. For high resolution sensors, especially those with no 'black' bands over turbid waters, the corrections for these effects should be separated from the atmospheric correction. Similarly, pixel identification is a challenge, especially for floating objects and shadows. Cloud shadowing not only impacts the earth's surface, but also the atmosphere between the cloud and its shadow, which could lead to erroneous results in that area. Novel methods are required to tackle these issues.
- Pléiades has a panchromatic channel like many other land sensors, which could be useful for increasing the spatial resolution ("pan-sharpening") of the output products. There may be value in the high spatial resolution for improving pixel identification, and this could also be useful in detecting waves and hence in glint correction schemes.
- The algorithm presented here avoids adjacency effects to some degree in the atmospheric correction by selecting the darkest band dynamically. The resulting ρ_s will still be impacted by adjacency effects, and the method shows some promise for a brute-force estimation of (NIR band) adjacency effects in the residual between ρ_{dark} and the estimated ρ_{path}.

Acknowledgments

This work was funded by the Federal Belgian Science Policy Office (BELSPO) under the STEREO III programme PONDER project (SR/00/325). The Belgian Pléiades Archive is thanked for distribution of images used in this work. The operators of the Zeebrugge/MOW1 AERONET-OC station, Dimitry Van der Zande, and the Brussels/RMI AERONET station, Christian Hermans, are kindly thanked for their efforts in keeping the stations running and for the use of their data. Bouchra Nechad is thanked for providing Pléiades band specific calibration coefficients for her turbidity algorithm. The steering committee members of the PONDER project are thanked for their inputs and discussions. Three anonymous reviewers and the associate editor are thanked for comments which helped improve the manuscript.

Appendix A. Supplementary data

Supplementary data to this article can be found online at https://doi.org/10.1016/j.rse.2018.07.015.

References

Baeye, M., Quinn, R., Deleu, S., Fettweis, M., 2016. Detection of shipwrecks in ocean colour satellite imagery. J. Archaeol. Sci. 66, 1–6.
Barnes, B.B., Hu, C., Kovach, C., Silverstein, R.N., 2015. Sediment plumes induced by the Port of Miami dredging: analysis and interpretation using Landsat and MODIS data. Remote Sens. Environ. 170, 328–339.
Brando, V., Braga, F., Zaggia, L., Giardino, C., Bresciani, M., Matta, E., Bellafiore, D., Ferrarin, C., Maicu, F., Benetazzo, A., et al., 2015. High-resolution satellite turbidity and sea surface temperature observations of river plume interactions during a significant flood event. Ocean Sci. 11 (6), 909.
Chavez, P.S., 1988. An improved dark-object subtraction technique for atmospheric scattering correction of multispectral data. Remote Sens. Environ. 24 (3), 459–479.
Chen, J., Zhu, W., Tian, Y.Q., Yu, Q., Zheng, Y., Huang, L., 2017. Remote estimation of colored dissolved organic matter and chlorophyll-a in Lake Huron using Sentinel-2 measurements. J. Appl. Remote. Sens. 11 (3), 036007.
Concha, J.A., Schott, J.R., 2016. Retrieval of color producing agents in Case 2 waters using Landsat 8. Remote Sens. Environ. 185, 95–107.
Dorji, P., Fearns, P., 2017. Impact of the spatial resolution of satellite remote sensing sensors in the quantification of total suspended sediment concentration: a case study in turbid waters of Northern Western Australia. PloS one 12 (4), e0175042.
Doxaran, D., Castaing, P., Lavender, S., 2006. Monitoring the maximum turbidity zone and detecting fine-scale turbidity features in the Gironde estuary using high spatial resolution satellite sensor (SPOT HRV, Landsat ETM+) data. Int. J. Remote Sens. 27 (11), 2303–2321.
European Commission, 2000. Directive 2000/60/EC of the European Parliament and of the Council of 23 October 2000 establishing a framework for community action in the field of water policy. Off. J. Eur. Communities 43, 1–73.
Fettweis, M., Matthias, B., Francken, F., Van den Eynde, D., 2016. MOMO activiteitsrapport (1 januari–30 juni 2016).
Franz, B.A., Bailey, S.W., Kuring, N., Werdell, P.J., 2015. Ocean color measurements with the Operational Land Imager on Landsat-8: implementation and evaluation in SeaDAS. J. Appl. Remote. Sens. 9 (1) 096070-096070.
Fritz, C., Dörnhöfer, K., Schneider, T., Geist, J., Oppelt, N., 2017. Mapping submerged aquatic vegetation using RapidEye satellite data: the example of Lake Kummerow (Germany). Water 9 (7), 510.
Gao, B.-C., Montes, M.J., Li, R.-R., Dierssen, H.M., Davis, C.O., 2007. An atmospheric correction algorithm for remote sensing of bright coastal waters using MODIS land and ocean channels in the solar spectral region. IEEE Trans. Geosci. Remote Sens. 45 (6), 1835–1843.
Gernez, P., Doxaran, D., Barillé, L., 2017. Shellfish aquaculture from space: potential of Sentinel2 to monitor tide-driven changes in turbidity, chlorophyll concentration and oyster physiological response at the scale of an oyster farm. Front. Mar. Sci. 4, 137.
Gordon, H.R., Brown, J.W., Evans, R.H., 1988. Exact Rayleigh scattering calculations for use with the Nimbus-7 coastal zone color scanner. Appl. Opt. 27 (5), 862–871.
Gordon, H.R., Wang, M., 1994. Retrieval of water-leaving radiance and aerosol optical thickness over the oceans with SeaWiFS: a preliminary algorithm. Appl. Opt. 33 (3), 443–452.
Hedley, J.D., Roelfsema, C.M., Chollett, I., Harborne, A.R., Heron, S.F., Weeks, S., Skirving, W.J., Strong, A.E., Eakin, C.M., Christensen, T.R., et al., 2016. Remote sensing of coral reefs for monitoring and management: a review. Remote Sens. 8 (2), 118.
Ho, J.C., Stumpf, R.P., Bridgeman, T.B., Michalak, A.M., 2017. Using Landsat to extend the historical record of lacustrine phytoplankton blooms: a Lake Erie case study. Remote Sens. Environ. 191, 273–285.
Kaufman, Y.J., Wald, A.E., Remer, L.A., Gao, B.-C., Li, R.-R., Flynn, L., 1997. The MODIS 2.1-/spl mu/m channel-correlation with visible reflectance for use in remote sensing of aerosol. IEEE Trans. Geosci. Remote Sens. 35 (5), 1286–1298.
Kotchenova, S.Y., Vermote, E.F., Matarrese, R., Klemm Jr, F.J., 2006. Validation of a vector version of the 6S radiative transfer code for atmospheric correction of satellite data. Part I: path radiance. Appl. Opt. 45 (26), 6762–6774.
Kutser, T., Metsamaa, L., Strömbeck, N., Vahtmäe, E., 2006. Monitoring cyanobacterial blooms by satellite remote sensing. Estuar. Coast. Shelf Sci. 67 (1), 303–312.
Kutser, T., Paavel, B., Verpoorter, C., Ligi, M., Soomets, T., Toming, K., Casal, G., 2016. Remote sensing of black lakes and using 810 nm reflectance peak for retrieving water quality parameters of optically complex waters. Remote Sens. 8 (6), 497.
Lyzenga, D.R., Malinas, N.P., Tanis, F.J., 2006. Multispectral bathymetry using a simple physically based algorithm. IEEE Trans. Geosci. Remote Sens. 44 (8), 2251–2259.
Matthews, M.W., Bernard, S., Winter, K., 2010. Remote sensing of cyanobacteria-dominant algal blooms and water quality parameters in Zeekoevlei, a small hypertrophic lake, using MERIS. Remote Sens. Environ. 114 (9), 2070–2087.
Mélin, F., Sclep, G., 2015. Band shifting for ocean color multi-spectral reflectance data. Opt. Express 23 (3), 2262–2279.
Moran, M.S., Bryant, R., Thome, K., Ni, W., Nouvellon, Y., Gonzalez-Dugo, M., Qi, J., Clarke, T., 2001. A refined empirical line approach for reflectance factor retrieval from Landsat-5 TM and Landsat-7 ETM+. Remote Sens. Environ. 78 (1), 71–82.
Mumby, P.J., Edwards, A.J., 2002. Mapping marine environments with IKONOS imagery: enhanced spatial resolution can deliver greater thematic accuracy. Remote Sens. Environ. 82 (2), 248–257.

Nechad, B., Ruddick, K., Neukermans, G., 2009. Calibration and validation of a generic multisensor algorithm for mapping of turbidity in coastal waters. In: SPIE Europe Remote Sensing, 74730H-74730H.
Nechad, B., Ruddick, K.G., Schroeder, T., Oubelkheir, K., Blondeau-Patissier, D., Cherukuru, R., Brando, V.E., Dekker, A.G., Clementson, L.A., Banks, A.C., et al., 2015. Coastcolour round robin datasets: a database to evaluate the performance of algorithms for the retrieval of water quality parameters in coastal waters. Earth Syst. Sci. Data 7, 319–348.
Novoa, S., Doxaran, D., Ody, A., Vanhellemont, Q., Lafon, V., Lubac, B., Gernez, P., 2017. Atmospheric corrections and multi-conditional algorithm for multi-sensor remote sensing of suspended particulate matter in low-to-high turbidity levels coastal waters. Remote Sens. 9 (1), 61.
Ody, A., Doxaran, D., Vanhellemont, Q., Nechad, B., Novoa, S., Many, G., Bourrin, F., Verney, R., Pairaud, I., Gentili, B., 2016. Potential of high spatial and temporal ocean color satellite data to study the dynamics of suspended particles in a micro-tidal river plume. Remote Sens. 8 (3), 245.
Olmanson, L.G., Brezonik, P.L., Finlay, J.C., Bauer, M.E., 2016. Comparison of Landsat 8 and Landsat 7 for regional measurements of CDOM and water clarity in lakes. Remote Sens. Environ. 185, 119–128.
Pahlevan, N., Lee, Z., Wei, J., Schaaf, C.B., Schott, J.R., Berk, A., 2014. On-orbit radiometric characterization of OLI (Landsat-8) for applications in aquatic remote sensing. Remote Sens. Environ. 154, 272–284.
Roelfsema, C.M., Lyons, M., Kovacs, E.M., Maxwell, P., Saunders, M.I., Samper-Villarreal, J., Phinn, S.R., 2014. Multi-temporal mapping of seagrass cover, species and biomass: a semi-automated object based image analysis approach. Remote Sens. Environ. 150, 172–187.
Ruddick, K.G., De Cauwer, V., Park, Y.-J., Moore, G., et al., 2006. Seaborne measurements of near infrared water-leaving reflectance: the similarity spectrum for turbid waters. Limnol. Oceanogr 51 (2), 1167–1179.
Schläpfer, D., Hueni, A., Richter, R., 2018. Cast shadow detection to quantify the aerosol optical thickness for atmospheric correction of high spatial resolution optical imagery. Remote Sens. 10 (2), 200.
Snyder, J., Boss, E., Weatherbee, R., Thomas, A., Brady, D., Newell, C., 2017. Oyster aquaculture site selection using Landsat 8-derived sea surface temperature, turbidity, and chlorophyll a. Front Mar. Sci 4, 190.
Sterckx, S., Knaeps, E., Ruddick, K., 2011. Detection and correction of adjacency effects in hyperspectral airborne data of coastal and inland waters: the use of the near infrared similarity spectrum. Int. J. Remote Sens. 32 (21), 6479–6505.
Stumpf, R.P., Holderied, K., Sinclair, M., 2003. Determination of water depth with high-resolution satellite imagery over variable bottom types. Limnol. Oceanogr. 48 (1; NUMB 2), 547–556.
Thuillier, G., Hersé, M., Labs, D., Foujols, T., Peetermans, W., Gillotay, D., Simon, P., Mandel, H., 2003. The solar spectral irradiance from 200 to 2400 nm as measured by the SOLSPEC spectrometer from the ATLAS and EURECA missions. Sol. Phys. 214 (1), 1–22.
Toming, K., Kutser, T., Laas, A., Sepp, M., Paavel, B., Nõges, T., 2016. First experiences in mapping lake water quality parameters with Sentinel-2 MSI imagery. Remote Sens. 8 (8), 640.
Torbick, N., Ziniti, B., Stommel, E., Linder, E., Andrew, A., Caller, T., Haney, J., Bradley, W., Henegan, P.L., Shi, X., 2017. Assessing cyanobacterial harmful algal blooms as risk factors for amyotrophic lateral sclerosis. Neurotox. Res. 1–14.
Vanhellemont, Q., Neukermans, G., Ruddick, K., 2014. Synergy between polar-orbiting and geostationary sensors: remote sensing of the ocean at high spatial and high temporal resolution. Remote Sens. Environ. 146, 49–62.
Vanhellemont, Q., Ruddick, K., 2014. Turbid wakes associated with offshore wind turbines observed with Landsat 8. Remote Sens. Environ. 145, 105–115.
Vanhellemont, Q., Ruddick, K., 2015a. Advantages of high quality SWIR bands for ocean colour processing: examples from Landsat-8. Remote Sens. Environ. 161, 89–106.
Vanhellemont, Q., Ruddick, K., 2015b. Assessment of Sentinel-3/OLCI sub-pixel variability and platform impact using Landsat-8/OLI. In: Ouwehand, L. (Ed.), S-3 for Science Workshop, Proceedings of a workshop held 2–5 June, 2015 in Venice, Italy, pp. 77 ESA SP-734, ISBN 978-92-9221-298-8.
Vanhellemont, Q., Ruddick, K., 2016. ACOLITE For Sentinel-2: aquatic applications of MSI imagery. In: ESA Special Publication. Presented at the ESA Living Planet Symposium held in Prague, Czech Republic.
Vanlede, J., Dujardin, A., 2014. A geometric method to study water and sediment exchange in tidal harbors. Ocean Dyn. 64 (11), 1631–1641.
Vermote, E., Tanré, D., Deuzé, J., Herman, M., Morcrette, J., Kotchenova, S., 2006. Second simulation of a satellite signal in the solar spectrum-vector (6SV). 6S User Guide Version. 3. pp. 1–55.
Vincent, R.K., Qin, X., McKay, R.M.L., Miner, J., Czajkowski, K., Savino, J., Bridgeman, T., 2004. Phycocyanin detection from LANDSAT TM data for mapping cyanobacterial blooms in Lake Erie. Remote Sens. Environ. 89 (3), 381–392.
Wang, M., 2007. Remote sensing of the ocean contributions from ultraviolet to near-infrared using the shortwave infrared bands: simulations. Appl. Opt. 46 (9), 1535–1547.
Wang, M., Shi, W., 2005. Estimation of ocean contribution at the MODIS near-infrared wavelengths along the east coast of the US: two case studies. Geophys. Res. Lett. 32 (13).
Wynne, T.T., Stumpf, R.P., Tomlinson, M.C., Dyble, J., 2010. Characterizing a cyanobacterial bloom in western Lake Erie using satellite imagery and meteorological data. Limnol. Oceanogr. 55 (5), 2025–2036.
Zibordi, G., Mélin, F., Berthon, J.-F., Holben, B., Slutsker, I., Giles, D., D'Alimonte, D., Vandemark, D., Feng, H., Schuster, G., et al., 2009. AERONET-OC: a network for the validation of ocean color primary products. J. Atmos. Ocean. Technol. 26 (8), 1634–1651.
Zibordi, G., Mélin, F., Berthon, J.-F., Talone, M., 2015. In situ autonomous optical radiometry measurements for satellite ocean color validation in the western black sea. Ocean Sci. 11 (2), 275–286.